The Effect of Cooling Rate on the Solidification of INCONEL 718

T. ANTONSSON and H. FREDRIKSSON

The superalloy INCONEL 718 (IN718) is a commonly used material in aerospace and turbine components. The advantage of this type of material with sluggish precipitation-hardening kinetics is that IN718 is readily weldable. Both wrought and cast parts are used and welded together. While the alloy has been studied previously, new production processes such as laser treatment demand better knowledge of the solidification process in IN718, especially at high cooling rates. In this investigation, the solidification process was studied over a wide range of cooling rates by three different experimental techniques: differential thermal analysis (DTA), mirror furnace (MF), and levitation casting. The solidification sequence and the reaction temperatures were identified. The microstructure and the change in growth morphology were also studied. Segregation measurements were performed, and the distribution of Nb was analyzed in detail for the different types of samples, because of its strong impact on the solidification sequence and microstructure. New observations are that the latent heat decreases and the effective partition coefficient increases with increasing cooling rate. The diffusion rate also seems to be enhanced in the first part of primary solidified dendrites. It is suggested that the new observations can be explained by an increased number of lattice defects formed in the solid as the cooling rate increases.

I. INTRODUCTION

SUPERALLOYS have been developed over the last 50 years as the demand for materials with improved properties has grown. Several different alloys have been developed. One of the most common is INCONEL* 718 (IN718), which is

---

*INCONEL is a trademark of INCO Alloys International, Huntington Woods, WV.

---

often used in cast components. Those components are also often welded together or sometimes repaired by welding. The solidification process is, thus, very important, and it has been investigated a number of times.[1–11] However, during recent years, new experimental information about the solidification process has been established.[12,13] The experiments show that equilibrium thermodynamic models normally cannot describe the solidification process adequately. These new observations have been used to explain air-gap formation in mold castings[14] and hot-crack formation in iron-based alloys.[15] The aim of this work is to investigate the solidification process of the superalloy IN718 in order to determine if a new description of the solidification process, where the effect of lattice defects during solidification is considered,[12,13,14] can also be applied to this alloy. The aim is to subsequently use the data in order to analyze hot-crack formation in this alloy.

II. EXPERIMENTAL PROCEDURE

Three different experimental techniques have been used to produce samples solidified with different cooling rates. The methods used are normal differential thermal analyser (DTA)

with quenching facilities, a special mirror furnace (MF), and a levitation casting process. The cooling rates increase from that with the DTA apparatus, with a low cooling rate, to an intermediate cooling rate with the MF, and a very high cooling rate with the levitation casting equipment. By using these three different techniques, solidification of IN718 at cooling rates in the range 0.25 °C/s to 20000 °C/s has been investigated. The cooling rate of each sample was evaluated from the cooling curve of the individual sample before the start of solidification. Both the thermal and microstructural evolution during the solidification process have been evaluated and compared. Microsegregation and the distribution of the alloying elements have also been investigated.

A. Material Used and Chemical Composition

The Volvo Aero Corporation provided the material used in the experiments as the commercial alloy IN718, delivered by Allvac (Mouroe, N.C). The AMS specification for IN718 and the analyzed chemical composition are presented in Table I.

Even if the samples were taken from the same batch, there might be some variation due to macrosegregation and, therefore, the chemical composition was measured after processing of the different experiments performed. The chemical analysis was performed using scanning electron microscopy (SEM) at Volvo Aero Corporation. Selected elements were analyzed and the area of analysis was sometimes rather small, which might result in a slight deviation in the measurements. The levitation samples could have lost some Ti and Al during the processing, but there is no satisfactory explanation of the slightly lower Nb content other than that the microstructure was different in the levitation samples and there was a limited area of analysis.

B. Differential Thermal Analysis

The DTA method[16] is widely used to evaluate the heat-of-transformation and transformation temperatures. The

---

T. ANTONSSON, Ph.D., and H. FREDRIKSSON, Professor, are with the Casting of Metals Department, Royal Institute of Technology/KTH, S-100 44 Stockholm, Sweden. Contact e-mail: hassef@matpr.kth.se

Table I. Chemical Analysis of the IN718 Alloy Used

Element	AMS 5596A Standard Wt Pct	DTA Samples Measured Wt Pct	MF Samples Measured Wt Pct	Levitation Measured Wt Pct	Certificate Allvac Wt Pct
Ni	50.0 to 55.0	51.96	52.76	51.57	53.85
Cr	17.0 to 21.0	18.92	18.60	19.23	17.71
Fe	balance	19.20	18.65	19.84	18.33
Nb	4.75 to 5.50	5.37	5.27	4.84	5.12
Mo	2.80 to 3.30	2.83	2.90	2.76	2.88
Ti	0.65 to 1.15	0.89	1.01	0.88	0.97
Al	0.20 to 0.80	0.54	0.52	0.43	0.50
Co	1.00*	0.06	0.10	0.20	0.11
C	0.08*	—	—	—	0.02
Mn	0.35*	0.09	0.09	0.10	0.05
Si	0.35*	0.14	0.09	0.15	0.06
P	0.015*	—	—	—	0.006
S	0.015*	—	—	—	<0.003
B	0.006*	—	—	—	0.003
Cu	0.30*	—	—	—	0.04

*Maximum content.

equipment used was a Mettler DTA furnace, modified with a quenching device. The sample was inserted into an alumina crucible with a thermocouple placed in the center. A graphite block surrounded the alumina crucible containing the sample to ensure isothermal conditions. The temperature was measured by type-S thermocouples. The thermocouples were placed into the sample, in the graphite block, and in the furnace chamber. Purified argon gas was used as a protective atmosphere in the furnace during the experiments. In this investigation, a heating and cooling rate of 0.25 °C/s was used. In the DTA equipment, the solidification process could be interrupted at selected temperatures by quenching the samples into brine, here called the DTA-Q experiments. Samples have been quenched at 1324 °C, 1320 °C, 1294 °C, 1293 °C, 1243 °C, 1188 °C, and 1138 °C. An estimation of the cooling rate during quenching in brine gave a cooling rate orders-of-magnitude higher than the cooling rate during the experimental run. The primary solidification structure before quenching should, thus, be conserved well in the microstructure.[23] A total of eight DTA-Q experiments and two complete DTA runs were performed.

The liquidus temperature was evaluated on heating from the DTA runs and was determined to be 1340 °C in the investigated alloy.

A typical cooling curve is presented in Figure 1. The undercooling was measured as the temperature difference before the start of solidification and the highest growth temperature. In all DTA samples, the undercooling was significant (approximately 13 °C in Figure 1) before the primary precipitation started and the recalesence was pronounced.

C. Mirror Furnace

In the mirror furnace[17] (MF), a small cylindrical sample with the dimension of 3 mm in diameter × 6 mm was heated and melted using two ellipsoidal lamps, as shown in Figure 2. The lamp filament is at one focal point of the reflector and the sample is at the other. In the center of the sample, a small type-B thermocouple was placed, for furnace regulation and temperature measurements. The sample was, finally, placed in an evacuated and sealed quartz glass tube. Intermediate
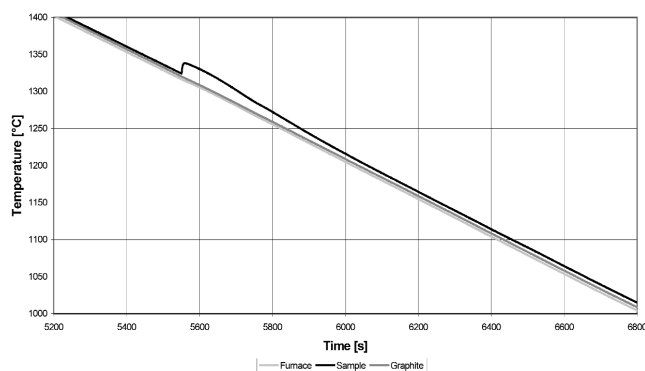

Fig. 1—A DTA cooling curve. The primary growth temperature is around 1337 °C after the recalesence, and the total solidification time is approximately 1000 seconds if the solidus temperature is 1075 °C. The liquidus temperature measured on heating was 1340 °C.
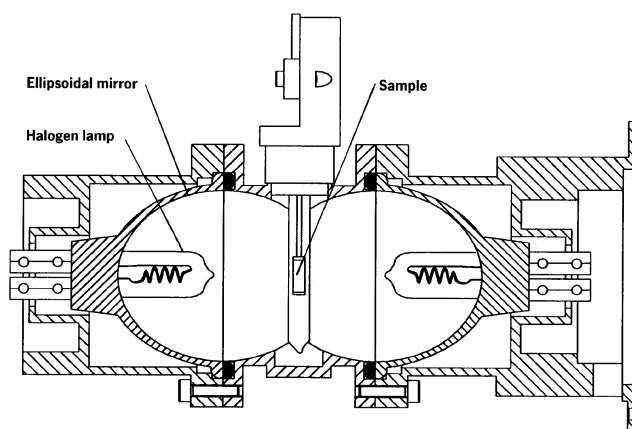

Fig. 2—Schematic cross section of the mirror furnace, showing the sample position.

cooling rates of approximately 10 °C/s to 200 °C/s can be achieved, depending on the external cooling conditions and the type of tube material surrounding the sample. It can produce a relatively homogeneous temperature distribution within
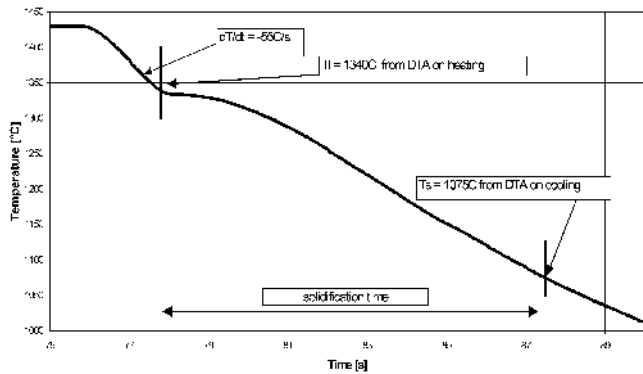
Fig. 3—Cooling curve for IN718 processed in the mirror furnace. The highest primary growth temperature is 1333 °C and the total solidification time is approximately 10 s.

the sample for most metals with a high thermal conductivity. This means that the Biot or Nu number is small, because of the small sample size at the cooling rates presented earlier. In this study, cooling rates in the liquid before solidification were around 75 °C/s with forced-gas cooling and around 55 °C/s without additional cooling. Six samples were processed. Two samples were studied in more detail, one with forced cooling and one without forced cooling.

A cooling curve for sample 2 is presented in Figure 3. No undercooling before primary precipitation and growth was found, as can be seen in Figure 3. This could be due to a favorable nucleation at the interface between the quartz tube and the melt. The cooling rate before the solidification starts was, in this case, evaluated to be 55.4 °C/s. The curve has a plateau at a temperature of 1333 °C. This gives a growth undercooling of 7 °C.

D. Levitation Technique

The levitation equipment consists of a 25 kVA Elphiac high-frequency generator with a specially designed levitation coil.[18] A water-cooled copper coil was built in a glass tube, in order to use a protective atmosphere of argon during melting and casting of the samples, as shown in Figure 4.

The sample weight was approximately 1.2 g. The sample was levitated and heated by the strong high-frequency magnetic field, and when the sample had melted and formed a spherical droplet, the power was turned off. The sample dropped and was cast in a platelike cavity in a copper mold with a size 1 × 10 mm. In the bottom at the center of the cavity, a thin, 0.1-mm-diameter, open type-S thermocouple registered the temperature during the solidification process. The mold and thermocouple are shown in Figure 5.

This equipment gives the highest cooling rate. The measured cooling rate in the liquid before solidification of the levitation-type samples was typically around 15,000 °C/s, measured from the slope of the cooling curve at the liquidus temperature. The sampling rate was approximately 5000/s. Seven samples were cast, but in three samples, either the casting or the temperature measurement were not satisfactory. This was caused by misalignment when the small droplet did not fall exactly into the center of the mold cavity without touching the upper mold wall. A cooling curve for a levitation sample is presented in Figure 6. The recales-
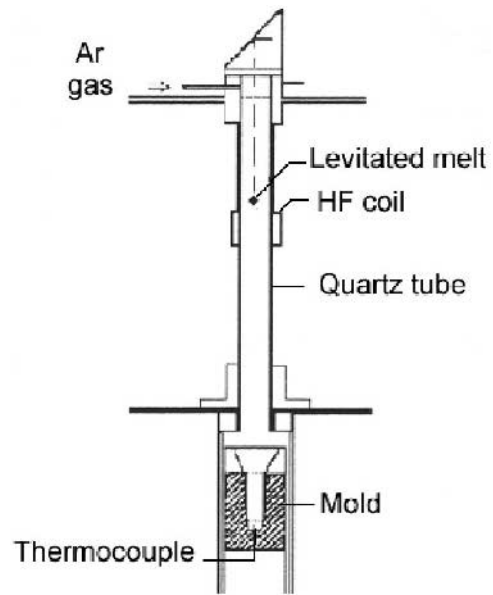

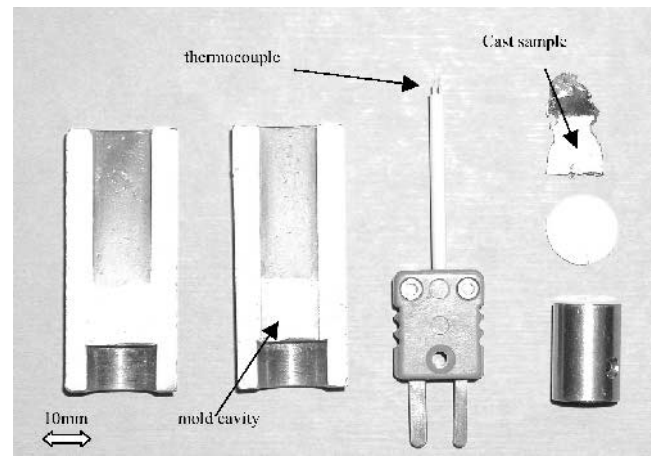Fig. 4—Schematic picture of the levitation equipment.

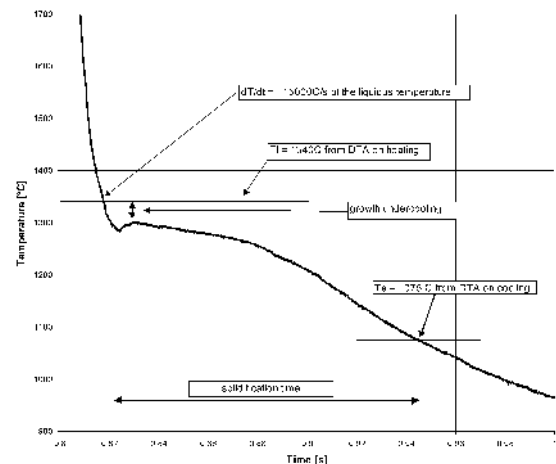Fig. 5—Photograph of the dissassembled levitation mold including the thermocouple and a cast sample.

Fig. 6—A levitation experiment cooling curve. There is an undercooling and recalesence, but the solidification temperature is around or below 1300 °C during the primary precipitation. The total solidification time is only about 0.1 s.

ence of the temperature curve is noticeable, and the highest growth temperature is around 1300 °C. This gives a growth undercooling of 40 °C, which is considerably larger, compared to that of 3 °C in the DTA and 7 °C in the MF samples. Two samples were studied in more detail, including microprobe measurements and heat-transfer calculations.

III. RESULTS

The solidification sequence and reaction temperatures in IN718 are dependent on the nominal alloy content. According to the AMS 5596A standard, the composition range of alloy IN718 is rather broad for many important elements, such as Nb, Ti, Al, and C, as shown in Table I. The amount of Ti, Nb, N, and C influences the precipitation of TiN particles and γ-NbC eutectic phase. Previous investigations[1–10] on the solidification of IN718 show differences in the liquidus temperature, solidus temperature, γ-NbC eutectic temperature, and Laves eutectic temperature. Variations in alloy compositions can, thus, give different results for the solidification temperatures and precipitation, as shown in Table II. The main feature of this investigation was to study the influence of the cooling rate on the solidification and not to simply perform another solidification study of IN718. The same base material with a given chemical composition was, thus, used in the different cooling-rate experiments.

The results of other investigators' measurements of the reaction temperatures are shown in Table II.

The further analysis is continued with the time-temperature recordings of the experiments together with the microstructure at the three different cooling rates. The first-order derivative of the sample temperature in a complete DTA run, as in Figure 1, was calculated and is shown in Figure 7. This was done in order to find the different reaction temperatures. This curve will be used subsequently when the microstructure formation is discussed.

A. Solidification Structure

The samples were cut, metallographically prepared, and analyzed in an optical microscope. The samples were etched with a mixture of HCl and HNO$_3$ using a mixing ratio of 5:1.

1. Microstructure of DTA samples

Figure 8 shows the microstructure in the completely solidified sample without quenching.

The structure consists of primary austenitic dendrites. TiN precipitates are observed inside the dendrites, while in the interdendritic regions, NbC and Laves phases can be seen. The solidification sequence will now be further analyzed in the quenched samples. In samples quenched at the highest temperatures of 1324 °C to 1293 °C, only primary γ-dendrites containing some small cubic TiN could be seen, together with quenched liquid, as shown in Figure 9.

In the sample quenched at 1243 °C, a number of NbC carbides could be observed at the border between the γ phase and the quenched liquid, as shown in Figure 10. This is a result of a divorced eutectic reaction.

The NbC carbide precipitation takes place between 1293 °C and 1243 °C. The reaction was identified on the thermographs (Figure 7), and the L $\rightarrow$ γ + NbC reaction temperature was found to begin at 1280 °C and to cease

Table II. Results from Different Investigators for the Reaction Temperatures in IN718

| Author	Eiselstein	Knorovsky	Cieselak	Fayman	Bouse	Ballantyne	Poole	Murata	Cao	Fomnenti	This investigation
Liquidus on heating	—	1364	1351	1345	1355	—	1341	—	1345	1340	1340
Liquidus on cooling	1260	—	—	1316	1330	1340	—	1360	1315	1330	1337
Solidus on heating	—	1320	1297	1281	1280	—	1243	—	—	1240	1250 to 1230
Solidus on cooling	1227	—	—	—	1240	1245	—	—	—	—	1075
Gamma/NbC eutectic on heating	—	1258	1230	1290 to 1225	—	—	1321 to 1271	—	1305 to 1267	1305 to 1270	—
Gamma/NbC eutectic on cooling	—	—	1257	1245 to 1225	—	1270	—	1290	1262	1280 to 1250	1280 to 1265
Gamma/Laves eutectic on heating	—	—	—	—	—	—	1177 to 1149	—	1167	—	—
Gamma/Laves eutectic on cooling	1177	1198	1185	1155 to 1120	1165	1173 to 1140	—	1160	1162	1172	1160 to 1075
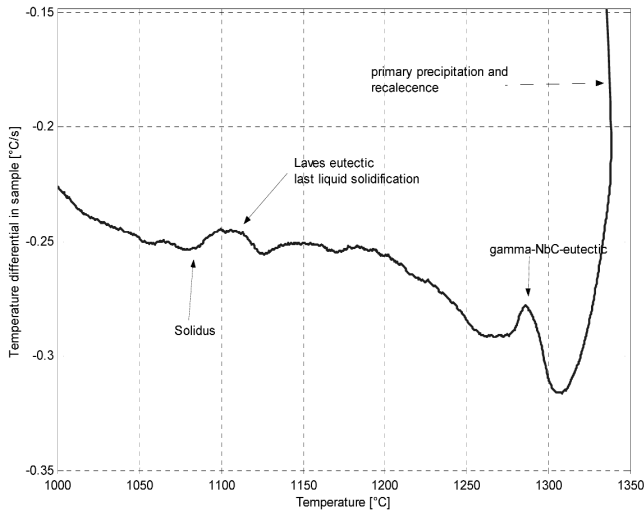
Fig. 7—The first-order derivative of the temperature of the sample, showing the reaction temperatures.

Fig. 9—Microstructure in a sample quenched at 1293 °C. NbC eutectic is only seen in areas with quenched liquid.
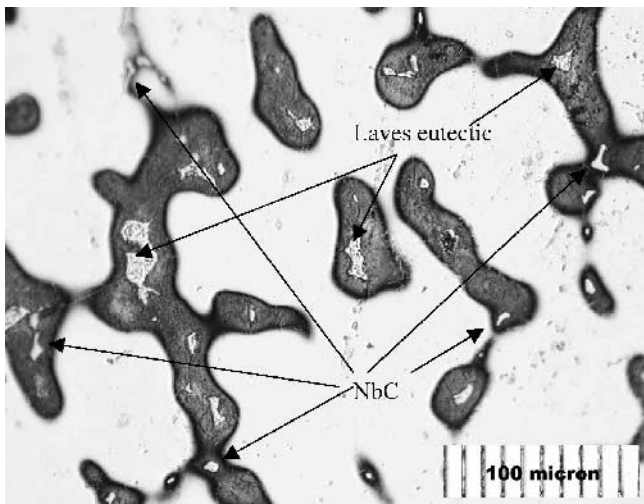

Fig. 8—Deep-etched microstructure of a DTA sample. In the center, a Laves eutectic area, formed in the last interdendritic melt, can be seen. Niobium carbides are also visible. The dark areas have high Nb content and have thus been etched aggressively, but this is still the same austenitic phase as the white primary precipitated dendritic areas.

Fig. 10—Microstructure in a sample quenched at 1243 °C. Niobium carbides can now be seen. The amount of quenched liquid is still significant.

at 1265 °C. The microstructure in the sample quenched at 1188 °C was not significantly different from the sample quenched at 1243 °C, but the amount of γ phase had increased. In the sample quenched at the lowest temperature of 1138 °C, quenched liquid could still be found in some interdendritic areas. Most of the interdendritic areas had changed their microstructure in the border between the γ phase and the remaining liquid, indicating that the Laves eutectic reaction had begun. The Laves eutectic reaction begins between 1188 °C and 1138 °C. According to the microstructure in the quenched samples and the thermograph, the Laves eutectic is precipitated over a temperature interval. This proves the following reaction: L + NbC → Laves + γ. In the microstructure, the Laves phase is precipitated as distinct "islands" in the interdendritic areas, usually with no connection to Nb carbides. The structure gives the impression that the fraction of NbC decreases
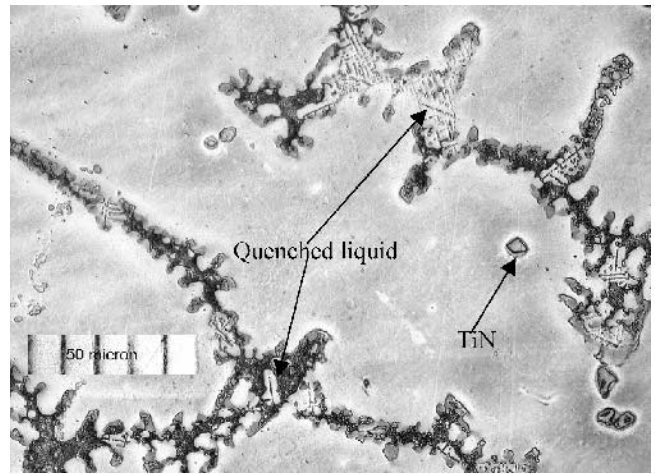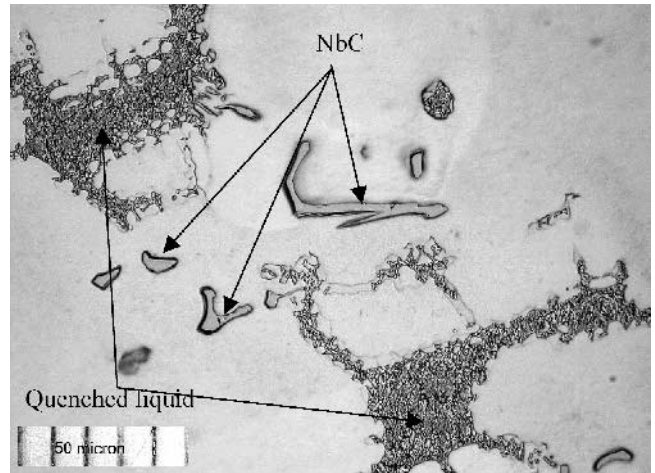
during the precipitation of Laves phase; unfortunately, the fraction of NbC was small, and the statistical error in the measurements was too large to provide good evidence for a decrease in the fraction of NbC.

The carbide formation continues below 1265 °C, but very few new carbides are nucleated, and the process is dominated by growth on already existing carbides. The fast eutectic reaction probably ceases when the liquid is depleted enough in carbon to reach the solubility limit of NbC. The solidification sequence will result in a final solidus temperature around 1075 °C (Figure 7).

The combined information from the DTA thermographs and the microstructures of the DTA-Q samples gives the following solidification sequence for IN718 at low (0.25 °C/s) solidification rates:

(1) L → TiN (s)   above liquidus
(2) L → γ 1340 °C
(3) L → γ + NbC   1280 °C to 1265 °C
(4) L + NbC → γ + Laves   1160 °C
(5) L → γ + Laves   1160 °C to 1075 °C

The precipitation temperatures can be influenced by nucleation. TiN does not seem to nucleate primary austenitic γ phase, because of the large undercooling with TiN particles already present in the melt. When analyzing "carbides," the NbC carbides sometimes are nucleated on TiN particles. Many of the TiN particles have small nuclei of Al_2O_3 or some other oxide in the center. Slag inclusions or refractories in the melt can, therefore, nucleate TiN, which, in turn, can aid the $L \rightarrow \gamma + NbC$ reaction. Nucleation difficulties of NbC can, on the other hand, depress the $L \rightarrow \gamma + NbC$ reaction to lower temperatures.

The volume fraction of quenched liquid was evaluated by random-line measurement on the sample in optical-microscope pictures of each quenched sample. The result is presented as points in Figure 11. Those measurements will be used and compared with values calculated later.

2. Microstructure of MF samples

In the MF samples, the microstructure was much finer than in the DTA samples but with the same type of microstructure, as shown in Figure 12. This figure shows that the matrix consists of γ-dendrites with NbC and Laves phase in the interdendritic regions. Some TiN particles were also observed. The particles are small and were analyzed in more detail by SEM.

3. Microstructure of levitation-cast samples

In the levitation samples, the microstructure was very fine. Columnar dendritic crystals had grown from the surface into the middle of the sample, as shown in Figure 13. The primary dendrites started to grow in a fanlike pattern from nucleation sites at the surface, as shown in Figure 14. In the vicinity of the nucleation points, the material seems to have undergone a diffusionless transformation which continued with a cell-like solidification.

Further inward into the sample, dendrite arms start to form, and a dendritic solidification pattern with almost constant dendrite-arm spacing continues to the center of the sample, as shown in Figure 15.
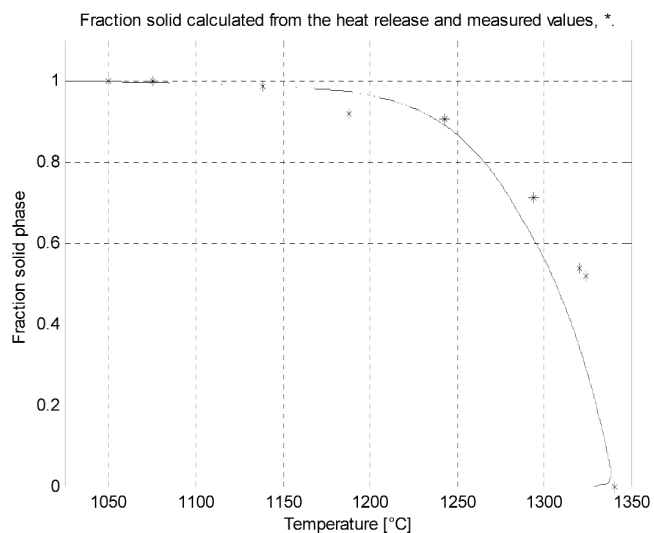
The secondary-dendrite-arm spacing was measured (Figure 16). Close to the surface, the spacing is found to be 1.5 μm. At a distance of 125 μm, the secondary-dendrite-arm spacing
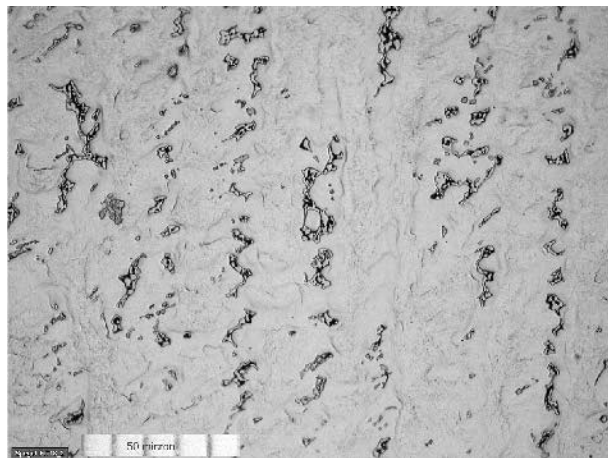

Fig. 12—Microstructure of an MF sample. Laves phase precipitation can be seen as the dark area in the interdendritic areas. NbC carbides are also present.
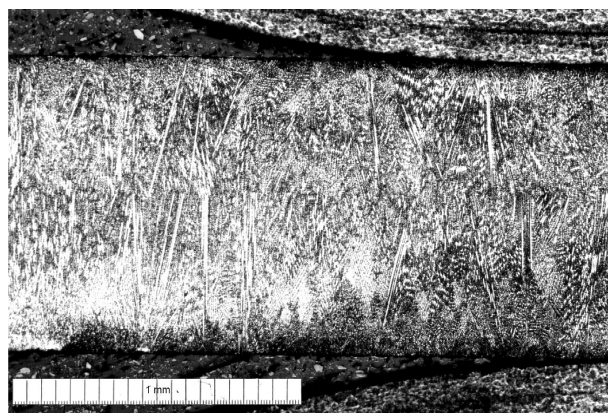

Fig. 13—A cross section of the levitation sample. Columnar dendrites have grown from the surface to the center of the sample.

Fig. 11—Measured solid fractions as a function of temperature (*) combined with the solid fraction calculated from the heat release balance in the thermal analysis. At the beginning of solidification, the calculated curve is curved, due to the undercooling and recalesence at the beginning of the solidification.
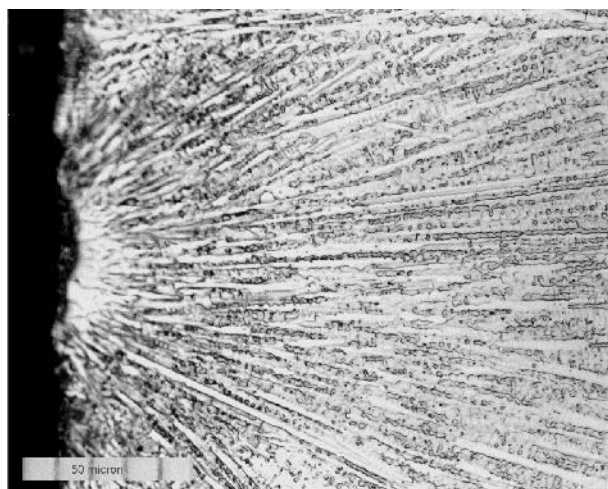

Fig. 14—The microstructure close to a nucleation site. Dendrites have grown in a fanlike pattern into the sample from the nucleation sites.
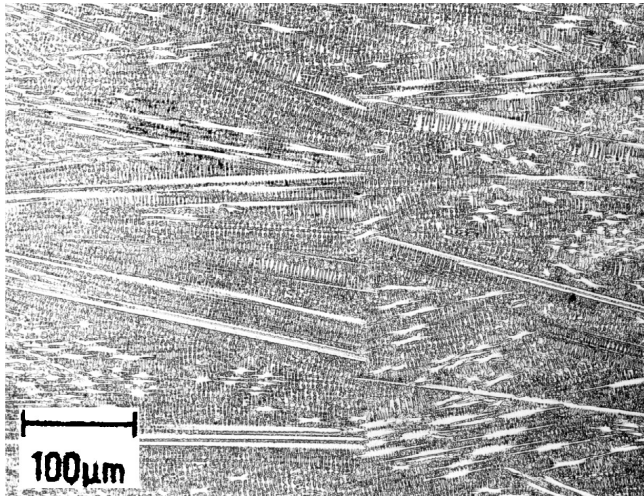
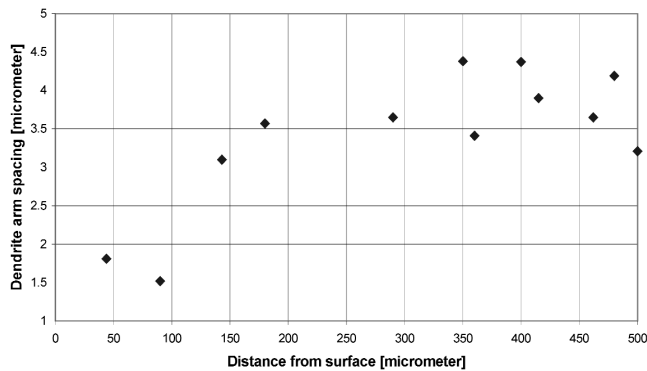Fig. 15—Microstructure of the central part of the levitation sample.

Fig. 16—Measured dendrite arm spacing from the surface to the center of the levitation sample. After approximately 150 μm, the dendrite arm spacing appears to be almost constant.

Fig. 17—The etched microstructure in a mirror furnace sample, showing a dendrite intersection and hardness marks. The chemical analysis was performed as point analysis straight across the dendrite, after removal of the etching.
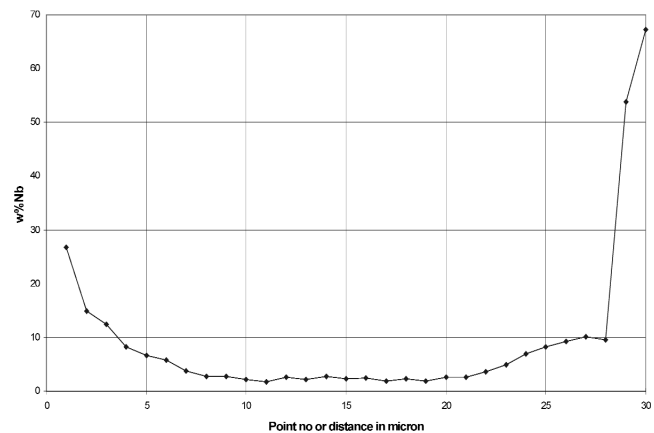

Fig. 18—The Nb concentration across the dendrite along the line in Fig. 17. Analysis was made at 30 points in this measurement. The distance between each point is approximately 1 μm.

suddenly increases to about 4 μm. The secondary-dendrite-arm spacing is constant into the center. Some NbC was found in the interdendritic regions. However, no Laves phase could be observed. The fraction of NbC, estimated to be less than 1 pct, is smaller than in the DTA and MF samples.

B. *Segregation and Microprobe Measurements*

Microprobe measurements have been performed in every type of sample. All elements except C and N were analyzed. Nb is one of the most important elements; due to its formation of NbC and Laves phase, it is also one of the elements which segregates most. It has the strongest impact on both the solidification sequence and microstructure. Only the Nb segregation will be discussed in more detail.

The measurements over dendrite intersections were performed by etching the samples to find suitable dendrite areas for study. Hardness marks were made on both sides of the dendrite cross, and the etching was polished away (Figure 17). Point analysis in a line across the dendrite was, thereafter, performed. Figure 18 shows the result of the measurement over the intersection in Figure 17.

The lowest values of the Nb concentration in the middle of the dendrite, which represents the first solidified part

of the primary dendrite arm, were used to calculate a mean minimum value. The lowest mean value of the Nb concentration in the dendrite cores was evaluated by taking the average value of three measurements in each of two different MF samples and of three measurements in each of two different levitation samples. The mean values obtained as a function of cooling rate are presented in Figure 20.

In the levitation samples, no segregation could be resolved by chemical analysis in the "white spots" close to the nucleation sites. This fact, combined with the uniform etching of these areas, makes a difusionless transformation probable at these high cooling rates (Figure 19).

When analyzing the results from the Nb segregation, two different observations were made. Figure 20 shows the lowest mean concentration of Nb in the central part of the dendrite arms as a function of the cooling rate. The figure shows that the Nb content in the dendritic cores increased with increased cooling rate. The effect will be more pronounced if the result is presented in the form of an efficiency partition coefficient (k^e). This partition coefficient is calculated
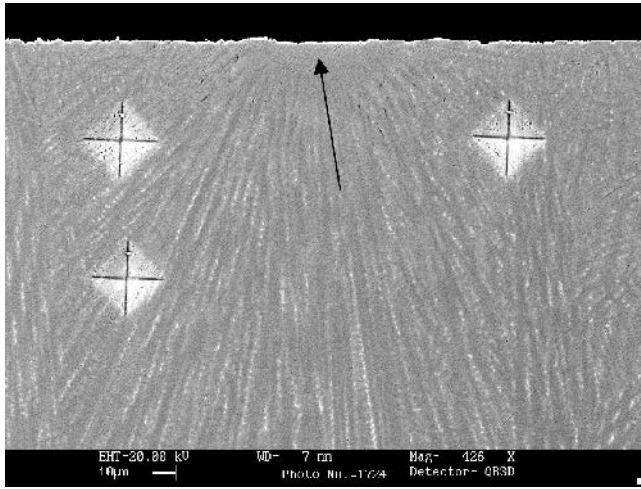
Fig. 19—A SEM backscattered electron image of a "nucleation" site, indicated by the arrow, in one of the levitation samples. No chemical segregations could be resolved in this area in the vicinity of the sample surface (top). The crosses are hardness marks to locate the area of interest in the sample.
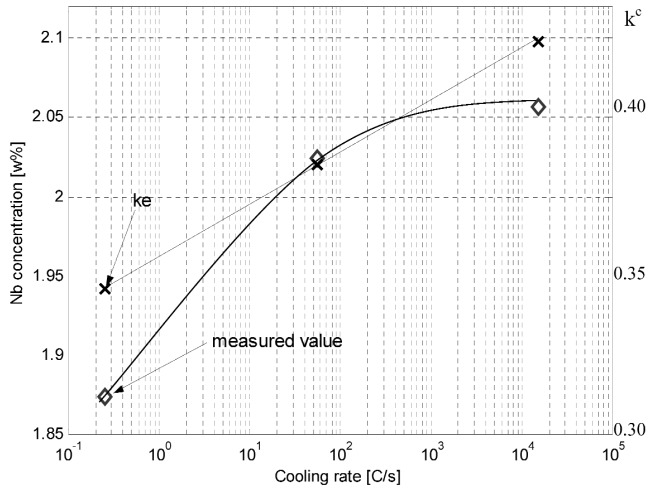

Fig. 20—Minimum Nb concentration in dendrite core as a function of cooling rate. The Nb concentration increases with cooling rate. Each point represents the lowest mean Nb concentration of several measurements over a minimum of three dendrite crosses in each type of sample. k^e is C_{meas}/C^0.

by dividing the measured data by the average composition, given in Table I. The result is shown in Figure 20 as well. The conclusion from this plot is that it increases faster at higher cooling rates than the measured data show.

The Nb concentration in the dendrite cores in the quenched samples was also measured. Several dendrite intersections were measured in each quenched sample. It was observed that the Nb content in the dendrite cores increased during the solidification process, as shown in Figures 21 and 24. The Nb increase in the dendrite cores during the solidification time is an indication of a slight backdiffusion of Nb in the primary austenitic phase; this will be discussed later. The average Nb content in the quenched liquid was also measured, and the result is also presented in Figure 21. This
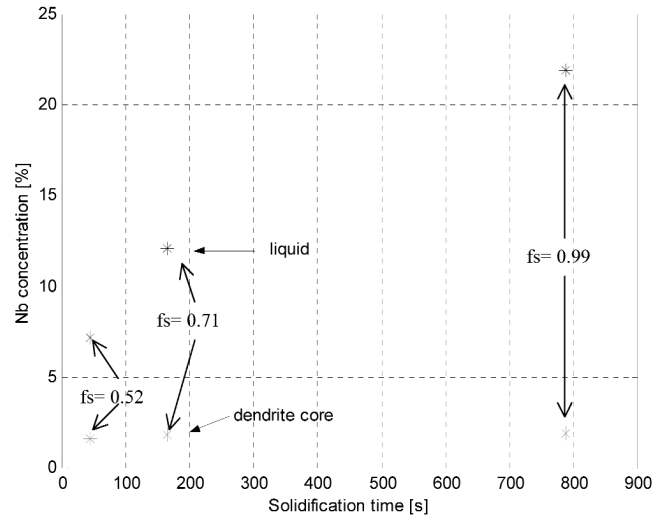

Fig. 21—The Nb concentration in DTA-Q samples quenched at different temperatures. The Nb is greatly enriched in the liquid and the concentration in the dendritic core increases from 1.64 to 1.87 pct during 795 s of solidification. This is an indication of backdiffusion of Nb during the solidification process. The measured solid fraction, fs, in the samples are 0.52, 0.71, and 0.99.

measurement was performed, in at least two places in each type of sample, as a chemical mean value of elements over an area of quenched liquid.

Figure 21 shows that in the DTA-Q samples, the Nb content in the quenched liquid increased from 7.2 pct Nb at 1324 °C, to 12.11 pct Nb at 1294 °C, and to 21.89 pct Nb at 1138 °C. At 1138 °C, Laves eutectic has started to form, and it seems that the Nb concentration has to be above 20 pct for the formation of Laves eutectic. At the high cooling rate obtained in the levitation samples, the maximum Nb concentration in the interdendritic areas was always measured to be less than 19 pct Nb. This amount of Nb could be too low to form the Laves phases, which may be the reason that no Laves phase was found in these samples.

C. Evaluation of Solid Fraction and Latent Heat

From the DTA thermographs and the cooling curves from the MF and levitation experiments, the heat release and, thus, the latent heat of solidification could be calculated or estimated.

1. Calculations and evaluation of DTA samples

The latent-heat calculations were mainly based on the method without a standard used by Fredriksson and Rogberg.[19] In the calculations, it was assumed that the temperature gradient in the sample is small.

A heat balance was applied to the experiment. The mass of the sample and the mass of the crucible was considered.

The heat evolved in the sample is equal to the heat transported away from the sample:

$$\frac{dQ}{dt} = \left(m^{sample} c_p^{sample} + m^{crucible} c_p^{crucible} \right) \cdot \left(-\frac{dT_s}{dt} \right) + q \quad [1]$$

where m^{sample} is the mass of the sample, $m^{crucible}$ is the mass of the crucible, c_p^{sample} is the heat capacity of the sample,

c_p^{crucible} is the heat capacity of the crucible, and q is the heat evolved in the sample,

$$\text{where } q = \begin{cases} 0 & T > T_1 \\ m^{\text{sample}} \dfrac{df}{dt} \cdot (\Delta H) & T_1 < T > T_s \\ 0 & T < T_s \end{cases} \quad [2]$$

and the heat transfer from the sample:

$$\frac{dQ}{dt} = A\sigma\varepsilon(T_s^4 - T_f^4) + Ah(T_s - T_f) \quad [3]$$

where A is the area, σ is the Stefan–Boltzman constant, ε is the emissivity, h is the heat-transfer coefficient, T_s is the temperature of the sample, and T_f is the temperature of the furnace. If the temperature difference between the sample and the surrounding is small compared with the absolute temperature,

$$\frac{dQ}{dt} \approx (\delta' + \gamma' T_f^3) \cdot (T_s - T_f) \quad [4]$$

where $\delta' = Ah$ and $\gamma' = 4\sigma\varepsilon A$.

By combining these equations, the constants δ' and γ' could be calculated by evaluating the cooling rate of the sample compared with the temperature of the surrounding. When evaluating a DTA cooling curve without a standard sample, a reference curve is calculated. The reference curve (T_{ref}) should follow the temperature of the sample as if no solidification had taken place. A magnified section of the solidification curve with the different temperatures is shown in Figure 22.

The latent heat can now be calculated according to,

$$-\Delta H \approx \frac{m^{\text{sample}}c_p^{\text{sample}} + m^{\text{crucible}}c_p^{\text{crucible}}}{m^{\text{sample}}} \int\limits_{\text{start}}^{\text{end}} (\delta' + \gamma' T_{\text{gr}}^3) \cdot$$
$$(T_s - T_{\text{ref}}) \cdot dt \quad [5]$$

The treatment is valid if c_p is constant. The c_p value is not constant between the liquid and solid IN718, but the difference is not large.[24] The maximum error introduced will be Δc_p times the temperature interval during solidification. This err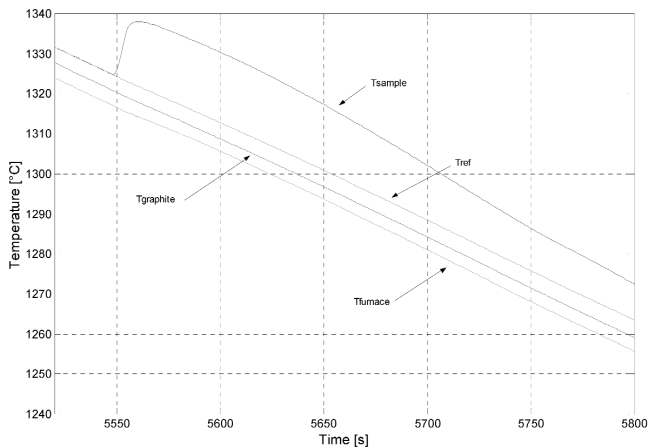or will be decreased, because a large amount of liquid is present at the beginning of solidification and the reference temperature has been slightly adjusted to the cooling after solidification had finished. The maximum error in the latent heat introduced by assuming a constant c_p value is estimated to be 10.2 kJ/kg.

2. *Latent heat evaluated from DTA*

The latent heat of solidification of IN718 has been calculated to be 241 ± 48 kJ/kg, with C_{p_1} = 720 J/kg K. The reference curve has been derived from the temperature measurements in the surrounding graphite. Richardsson *et al.*[20] measured the latent heat for IN718 to be 210 kJ/kg. Pottlacher *et al.*[21] reported the latent heat of solidification of IN718 to be 227 kJ/kg, performed by an unusual wire technique. Some other values seen in literature, for instance, the 295 kJ/kg value used by Nastac and Stefanescu,[22] are higher. The calculated value in this investigation is between the extremes given in the literature.

3. *Solid fraction compared to heat release in DTA-Q samples*

The fraction solidified (*f*) was calculated according to Reference 19.

$$f = \frac{\displaystyle\int_{t^{\text{start}}}^{t'} (\delta + \gamma T_f^3)(T_s - T_{\text{ref}})dt}{\displaystyle\int_{t^{\text{start}}}^{t^{\text{end}}} (\delta + \gamma T_f^3)(T_s - T_{\text{ref}})dt} \quad [6]$$

where *f* is the fraction of solidification heat evolved from the total amount of latent heat at time t'.

The measured solid fractions were then compared with the normalized fraction of solid from the heat release in the sample (Figure 9).

If the total amount of heat released at a specific solid fraction is divided by the total amount of heat released and compared with the measured solid fraction, the latent heat evolved for the solidified fraction can be calculated. This result is presented in Figure 23.

The figure shows that the latent heat evolved at the beginning of the solidification process is smaller than the published

Fig. 22—Recorded temperatures, T_{sample}, T_{furnace}, and T_{graphite}, and the calculated reference temperature, T_{ref}, during solidification of an IN718 sample in the DTA furnace.
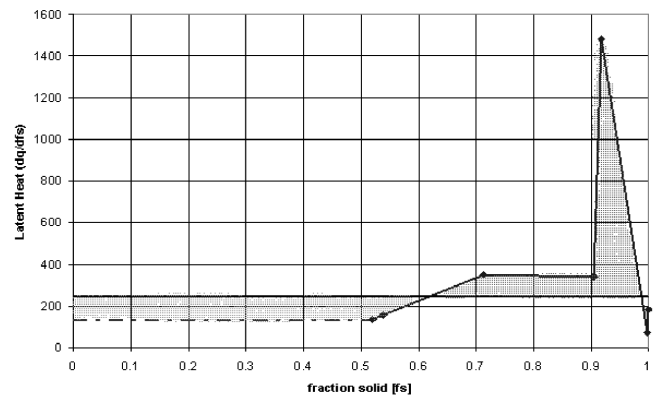

Fig. 23—The latent heat as a function of fraction solidified. The material solidified in the beginning must have a latent heat lower than the average, 241 kJ/kg, according to the heat release and the measured solid fraction.

values and higher at the end of the solidification process. However, the two areas are nearly equal. The explanation to this is that the rapid growth at the beginning of the solidification process gives a solid with a large fraction of lattice defects, which increase the energy of the solid. The defects will condense at the end of the process and increase the heat release.

One source of error could be that more solid phase grows on the primary dendrites during quenching. Pompe and Rattenmayr[23] have previously described this error. The measurement of the solid fraction is estimated to deviate by approximately 5 pct, because of measurement error in the manual evaluation. If solid is formed during quenching, the measured solid fractions should be consistently higher compared with the heat release, but the measurements are lower at high fractions of solid. The very high cooling rate of the sample when quenching into brine is expected to preserve the microstructure.

The formation of NbC eutectic could have a high heat of fusion, but the fraction of NbC is less than 4 pct, and the impact of the NbC-formation heat of fusion on the total heat of fusion must, thus, be small.

4. *Latent-heat evaluation from MF experiments*

In the MF, some estimates of the heat transfer from the samples must be made to be able to calculate the latent heat from the measured solidification curve. The assumptions made were as follows. (1) In the evacuated glass tube, the heat transfer along the sample and at the ends is negligible; only radial heat flow is, therefore, possible. (2) Before and after solidification, the glass tube and the sample have the same cooling rate.

The main heat resistance for heat release in the MF sample is the heat transfer between the outside of the thin glass tube and the gas in the furnace chamber. At high temperatures, heat transfer by radiation becomes more important. Although the sample and the gold-plated furnace are highly polished and they have very low emisivity, the influence of radiation cannot be neglected. By evaluating the cooling rate, combined with a heat balance at different temperatures before and after solidification, an effective heat-transfer coefficient could be calculated and fitted as a third-order polynomial as a function of temperature, thus including the effect of radiation. The calculated heat-transfer coefficient varied between 50 and 170 W/m^2 °C. This value seems reasonable for predominately convective heat transfer between the surface of the tube and the surrounding atmosphere. This value of the heat-transfer coefficient will also give a very small Nu number for the sample. The temperature gradient in the sample must, thus, be very small, and the temperature in the sample will be homogenous. By combining the heat-transfer coefficient with the heat balance, the surface temperature could be calculated, if the cooling rate of the glass tube is assumed to be the same as in the sample. This approximation could introduce an error in the calculations, but any discrepancy was considered to be small, as the energy difference due to a minor error in the temperature in the thin glass tube is small compared with the energy release in the sample during solidification.

The calculated latent heat in the MF sample was 193 ± 12 kJ/kg. This is a lower value than that obtained from the DTA samples. The accuracy of the calculated value is hard to estimate because of several unknown factors.

5. *Latent-heat evaluation from levitation experiments*

The latent-heat calculations of the levitation experiments are very difficult. The heat conductivity of the copper mold is very high ($k \approx 400$ J/sm K) compared with the IN718 cast sample ($k \approx 30$ J/sm K). In most mold-casting processes, heat transfer at the beginning of solidification, before a solid shell has formed, is high. When the solid shell has formed, an air gap usually forms between the casting and the mold due to the shrinkage of the casting. This air gap greatly reduces the heat transfer from the casting to the mold. In the treatment of the levitation samples, two extremes could be identified: good contact between the mold and the casting, and bad contact between the mold and the casting. In the first case, an analytical solution to the solidification could be applied. In these calculations, the solidification time was always less than 0.02 seconds. The measured solidification time varied between 0.08 and 0.1 seconds, which is about 5 times longer. The good-contact approach gave an interface temperature of approximately 350 °C, thus resulting in a very steep temperature gradient, ≈8000 °C/mm, in the vicinity of the sample surface. In the samples, the surface has a much finer microstructure and some parts even seem to have undergone a diffusionless transformation (the white spots). Local areas with the best contact are probably the sites for extreme undercooling, resulting in the white-spots nucleation sites. These observations show that there is partly good contact between the polished copper mold and the "semi" solid sample at the very beginning of the solidification. From the evaluation of the cooling curve, this time is estimated to be approximately 0.005 seconds.

After a solid shell has formed, the heat transfer drops dramatically and the major source for heat resistance will be in the air gap formed between the mold and the sample. The sample is small, and calculations of the heat transfer in the solid sample after solidification show that thermal contact between the mold and the sample is bad. With the small dimensions of the sample and with the heat conductivity of the mold and the sample, the Biots or Nusselt number will be small (Nu < 0.1). This will give a "Newtonian shape" of the cooling curve after the solidification is finished, which is also observed in the measurements. When the Nussel number becomes small, the solidification rate should be const██. The almost constant dendrite-arm spacing measured in the interior of the sample (Figure 13) indicates that the bad-contact assumption is valid after the formation of the solid shell.

It was not possible to evaluate the latent heat for the first solidified shell in the sample. The heat transfer varies with temperature, and locally good contact between the casting and the mold exists.

After the first solid shell has formed, the Nu number becomes small and the heat transfer equals that during cooling of the solid at 1075 °C. The heat release can be described by

$$Q = V \cdot \rho^s \cdot c_p^s \left(\frac{dT}{dt}\right)_{1075} \cdot t_s \approx \left(\rho \cdot V \cdot (-\Delta H) \cdot \frac{0.4}{0.5} + \rho \cdot V \cdot c_p \cdot \Delta T\right)$$

[7]

where ΔT is the temperature difference between the initial growth temperature and the solidus temperature.

The calculated latent heat of solidification ($-\Delta H$) in the levitation samples after recalescence was 187.5 ± 26 kJ/kg. This value is smaller than the value calculated from the DTA and MF measurements, and the latent-heat calculations overlap in the statistical interval. The calculation is rather approxi-

mate, but this suggests that the latent heat decreases at high cooling rates.

6. *Backdiffusion calculation and analysis*

Figure 18 presents microprobe measurements of the Nb content in the central part of the dendrite stem, together with measurements of the Nb content in the liquid as a function of the solidification time. The measurements show that the Nb content in the central part increases with solidification time. This may be a result of backdiffusion during the solidification process. A one-dimensional finite difference method (FDM) numerical solution to Fick's second law was applied to analyze this. A series of calculations were performed. First, the experimental data were compared to a calculation where a published diffusion coefficient[24] was used. The diffusion coefficient was then included as a function of temperature. The relation between temperature and time was fitted as an elliptical function from a complete experimental DTA run. The calculations were performed with the measured coarseness of the microstructure and by using a partition coefficient of 0.29. Two calculations are presented in Figure 24. One of the calculations shows that the backdiffusion is too slow when using the published value of the diffusion coefficient. The other calculation shows a better agreement with the experiments by assuming a higher diffusion rate at the beginning and the published diffusion coefficient at the end of the solidification process.

Figure 20 shows that the alloy content in the central part of a dendrite increased with the cooling rate. The backdiffusion model was also tested for this case. A rough estimation gives an approximately 10,000 times longer solidification time for the DTA samples compared with the levitation samples, but the dendrite-arm spacing was only approximately 16 times larger. This will, applying a rule of thumb (*e.g.*, the Einstein random-walk relation), result in a 40-times-longer backdiffusion in the DTA samples compared to the levitation samples. We conclude that there is no backdiffusion at the highest
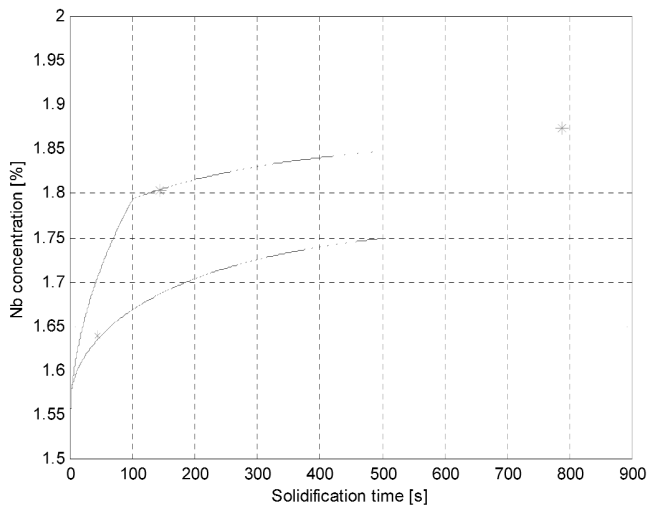
cooling rates. More ambitious calculations with the FDM solution have been made, which confirm the assumption of negligible backdiffusion, during the rapid solidification in the levitation samples. The measured high Nb content in the dendrite cores in the levitation samples cannot be explained by using published diffusion values combined with the measured coarseness of the microstructure. The nominal Nb content in the levitation samples was the lowest, but the measured Nb concentration in the dendrite cores was the highest, compared with the other samples, despite the fact that the backdiffusion should be negligible. The increase of the Nb content is, thus, an effect of the high solidification rates.

IV. DISCUSSION

Effects of the Cooling Rate on the Solidification

These experiments show that the solidification sequence and microstructure are not significantly affected by the cooling rate at low or medium cooling rates. The coarseness of the primary γ dendrites decreased with increasing cooling rate, but the microstructure was very similar, except for the length scale in the DTA and MF samples. At very high cooling rates, the primary dendrite shape is altered to a more cell-like form. At the highest solidification rates, a diffusionless transformation of the alloy seems to have taken place in the white spots in the levitation samples.

The nominal alloy content, thus, alters the precipitation temperatures and amount of secondary phases, for example, NbC and Laves phases.[1–10] Segregation of Nb is high and controls the solidification sequence together with interacting alloy elements, such as C. The cooling rate has an effect on the segregation of Nb. The measurements show an increased solubility in the primary γ phase of Nb with increasing cooling rate at the end of solidification. At the very high cooling rates obtained in the levitation samples, the interdendritic areas contained less Nb compared with the DTA and MF samples. No Laves phases could be found in the levitation samples. It is assumed be that the remaining Nb content of 16 pct by weight in the interdendritic areas was insufficient for Laves phase to form, due to a higher solubility in the γ phase. The result of the backdiffusion analysis indicates a higher diffusion coefficient in the beginning of the solidification than expected. The diffusion rate and/or the solubility of Nb in the γ phase must, thus, increase at higher cooling rates.

The latent heat also decreases with increasing cooling rate (Figure 25). The results in the experiments show an increased solubility of Nb, an increased diffusivity, a decreased latent heat, and a decreased growth temperature when the cooling rate increases. At very high cooling rates, the solidification sequence and microstructure change from dendrites, to cells, to a diffusionless transformation with increased cooling rate.

The experimental results are consistent with the experimental results and models discussed in a series of articles presented during the last ten years.[12,13] In this case, it has been observed that the latent heat decreases with increasing cooling rate. This is a result of an increase in the number of lattice defects in the solid phase. It will then influence the partition coefficient due to an interaction between the defects and the alloying elements, as earlier observed by Haddad–Sabzevar.[26] The number of defects will also affect the diffusion rate and increase this, according to our observations.

Fig. 24—Graph of measured Nb content in dendrite core (*) in the DTA samples quenched at different times. FDM backdiffusion calculations with published diffusion coefficient (lower line) are compared to calculations with a higher diffusion coefficient in the beginning of the solidification (upper line). A 5 times greater diffusion coefficient in the first part of the solidification process fits better with the measured values.
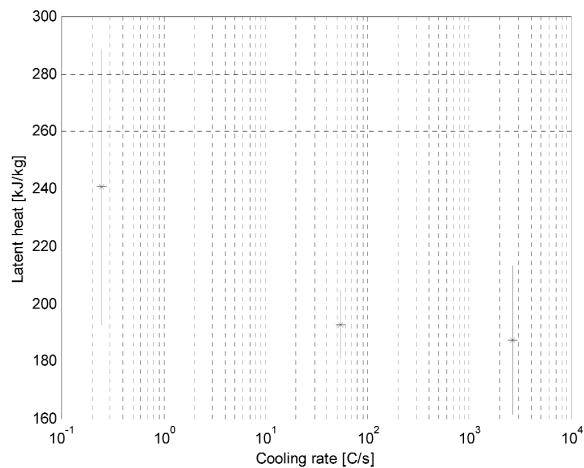
Fig. 25—Calculated latent heat for the different types of samples. The errors may be relatively large, but the calculations show a clear trend of decreasing latent heat during solidification with increasing cooling rate.

V. CONCLUDING REMARKS

A careful solidification analysis over a wide range of cooling rates has been performed. It was observed that the diffusion rate increases and that the effective partition coefficient also increases with increasing cooling rate. It is suggested that this can be explained due to an increased number of lattice defects formed in the solid state with increased solidification rate.

REFERENCES

1. H.L. Eiselstein: *ASTM STP 369*, ASTM, Philadelphia, PA, 1965, pp. 62-79.
2. G.A. Knorovsky, M.J. Cieslak, T.J. Headley, A.D. Romig, and W.F. Hammetter: *Metall. Trans. A*, 1989, vol. 20, pp. 1989-2149.
3. M.J. Cieslak and G.A. Knorovsky: *Superalloy 718, Metallurgy and Applications*, TMS, Warrendale, PA, 1989.
4. Y.C. Fayman: *Mater. Sci. Eng.*, 1987, vol. 92 (1–2), pp. 159-71.
5. G.K. Bouse: *Superalloy 718, Metallurgy and Applications*, TMS, Warrendale, PA, 1989, pp. 69-77.
6. A.S. Ballantyne, A. Michell, and J.F. Wadier: *Am. Vacuum Soc.*, 1980, pp. 599-623.
7. J.M. Poole: *Special Melting and Processing Technologies*, San Diego, CA, Apr. 11–15, 1988.
8. Y. Murata: *Superalloys 718, 625 and Various Derivatives*, TMS, Warrendale, PA, 1994.
9. W.D. Cao: *Superalloys 718, 625 and Various Derivatives*, TMS, Warrendale, PA, 1991.
10. A. Formenti and H. Fredriksson: "On the Solidification Behaviour of Ni-Base Superalloys IN718, IN625 and IN939," Internal Report, Metals Casting, Royal Institute of Technology, Stockholm.
11. J. Tinoco and H. Fredriksson: *High Temperatures Materials and Processes*, 2004, vol. 23, no. 1.
12. H. Fredriksson and T. Emi: *Mater. Trans., JIM*, 1998, vol. 39 (2), pp. 292-301.
13. J. Fjellstedt and H. Fredriksson: TRITA-MG-2001:08, ISRN-KTH:IMP-INR-01:08, Royal Institute of Technology, Stockholm, 2001; *Adv. Eng. Mater.*, 2003, vol. 5, no. 1-2, pp. 24-32.
14. J. Kron, T. Antonsson, and H. Fredriksson: *Int. J. Cast Met. Res.*, 2002, vol. 14, pp. 275-85.
15. H. Fredriksson and K. Hansson: TRITA-IIP-00-10, Royal Institute of Technology, Stockholm, unpublished research, Dec. 2000.
16. R.F. Speyer: *Thermal Analysis of Materials*, Marcel Dekker, Inc., New York, NY, 1994.
17. C. Lockowandt, K. Lŏth, L. Ekbom, A. Eliasson and A.E.W. Jarfoos: *Microgravity Applications Furnace Facility, MAFF, for Parabolic Flights.* The VIIIth European Symposium on Materials and Fluid Sciences in Microgravity, 12–16 April, 1992, Brussels, Belgium.
18. J. Liu: Thesis, Royal Institute of Technology, Stockholm, Sweden, 1989.
19. H. Fredriksson and B. Rogberg: *Metal Science*, The Metals Society, London, 1979, pp. 685-90.
20. M.J. Richardsson, D. Hayes, A.P. Day, and K.C. Mills: "MTS Programme on Processability, Thermophysical Data for Commercial Alloys Measured in PMP1, 2, and 3," National Physical Laboratory, Teddington, Middlesex, United Kingdom, 1996.
21. G. Pottacher, H. Hosaeus, E. Kaschnitz, and A. Seifer: *Scand. J. Metall.*, 2002, vol. 31, pp. 161-68.
22. L. Nastac and D.M. Stefanescu: *AFS Trans.*, 1996, vol. 104, pp. 425-34.
23. O. Pompe and M. Rattenmayr: *J. Cryst. Growth*, 1998. vol. 192, pp. 300-06.
24. K.C. Mills: "Recommended Values of Thermophysical Properties for Commercial Alloys.," Report, Centre for Materials Measurements and Technology, National Physical Laboratory, Teddington, Middlesex, United Kingdom.
25. *Smithells Metals Reference Handbook*, 7th ed., Butterworths, London, 1992.
26. M. Haddad-Sabzevar: Thesis, Royal Institute of Technology, Stockholm, 1994.